Available online at www.sciencedirect.com
SCIENCE DIRECT®
Journal of Computational Physics 188 (2003) 232–251
JOURNAL OF COMPUTATIONAL PHYSICS
www.elsevier.com/locate/jcp

The CASL algorithm for quasi-geostrophic flow in a cylinder

C. Macaskill [a,*], W.E.P. Padden [a], D.G. Dritschel [b]

[a] School of Mathematics and Statistics, University of Sydney, Sydney, NSW 2006, Australia
[b] Mathematical Institute, University of St. Andrews North Haugh, St. Andrews KY16 9SS, Scotland, UK

Received 26 June 2002; received in revised form 12 February 2003; accepted 6 March 2003

Abstract

The contour-advective semi-Lagrangian (CASL) algorithm is a hybrid Lagrangian–Eulerian numerical algorithm combining contour dynamics, for the advection of a materially conserved dynamical tracer, with spectral techniques, for the computation of the associated flow field. It benefits from the accuracy of contour dynamics, and the efficiency of spectral methods, and in applications to 'quasi-geostrophic' rotating, stratified flows, has no time-step restriction for numerical stability. It abandons the expensive aspect of contour dynamics – the computation of contour integrals to obtain the flow field – and the inaccurate (and costly) aspect of spectral methods – the advection of materially conserved tracers (requiring a time-step restriction for numerical stability and numerical diffusion). The two approaches are tied together by a fast method of converting tracer contours to gridded field values (Lagrangian → Eulerian) and the bi-linear interpolation of the flow field from the grid to points on the contours (Eulerian → Lagrangian). Here, we extend this method, originally developed for horizontally periodic flows, to flows within a cylindrical domain. Among other applications, this permits a comparison with experiments, which are often conducted in a cylindrical domain. We demonstrate the accuracy of the algorithm in a few test cases, then examine the differences between cylindrical and periodic domains for both simple vortex interactions and complex quasi-geostrophic turbulence.

AMS: 76B47; 65N35

Keywords: Vortex dynamics; Contour dynamics; Rotating stratified turbulence; CASL

1. Introduction

The study of oceanic vortex interaction, generation and dissipation poses a number of difficulties. The most significant is the fact that such vortices have typical scales of 50–100 km, and so are effectively inviscid, yet non-linear interactions give rise to an enstrophy cascade to small scales, limited in principle only by viscosity. Thus very high resolution is required to study such motions adequately.

* Corresponding author.
E-mail address: c.macaskill@maths.usyd.edu.au (C. Macaskill).

0021-9991/03/$ - see front matter
doi:10.1016/S0021-9991(03)00165-7

Both rotation and stratification play a crucial role in such motions. When rotation dominates, fluid motions tend to be approximately independent of the coordinate along the rotation axis, or two-dimensional (2-D), and vortices move as columns. When stratification dominates, fluid motions tend to be parallel to the approximately flat stratification surfaces, but vary strongly across such surfaces. In this case, motions are referred to as "layerwise 2-D", even though they depend on all three spatial coordinates. In both cases, the flow evolution depends only on the "horizontal" velocity, that which is perpendicular to the axis of rotation or the gradient of the stratification. These two important limiting cases have received much attention, particularly since they can be studied using 2-D models, or (in the case of stratification) discrete layer models, the simplest being a single layer of variable depth (e.g. [2,14,19,20,27,28,33]).

In practice, of course, flows in the ocean are constrained by both rotation and stratification. The latter suppresses vertical motions while the former weakens the variations of horizontal motions across stratification surfaces, in effect increasing vertical coherence. The local projection of the vorticity on the gradient of the stratification (i.e., of density), a scalar field known as the potential vorticity (PV), is conserved following this motion in the absence of dissipative or diabatic processes, and thus vortices are naturally defined by coherent regions of PV. The stability and interaction of such vortices has been used to understand the competing effects of rotation and stratification, and in particular to explain the often near equality of the vertical to horizontal scale ratio H/L and the rotational to buoyancy frequency ratio f/N ([11,12,30], and references therein).

The simplest model that retains the effects of rotation and stratification in a consistent way is the quasi-geostrophic (QG) model, first introduced more than 50 years ago and put on a firm asymptotic basis in the work of [3]. This model is based on leading-order hydrostatic and geostrophic balance (in which, respectively, the vertical and horizontal fluid acceleration is neglected in the momentum equations). This balance results in a linear relationship between the flow field and the PV, yet the evolution of PV – its advection – remains fundamentally non-linear. The flow field is recovered from the PV by inverting a 3-D Poisson equation, and it is this which induces vertical coupling between the PV advection in different layers or at different heights. This means that the detailed non-linear interaction of PV can be treated with a 2-D algorithm and yet the linear velocity (streamfunction) inversion requires a fully 3-D approach.

These characteristics make the contour dynamics method [5] particularly relevant, as this method has been shown to give extremely high resolution and accuracy in 2-D problems, corresponding here to each of the horizontal layers. The difficulty with contour dynamics has traditionally been the high cost of evaluating the integrals over PV contours from which the velocities are determined at each time-step. To a large extent this problem has been overcome in the CASL (contour advective semi-Lagrangian) method [7] where a dual approach is used: at each time-step the PV is interpolated onto a regular grid, and then a spectral approach is used to invert the Poisson equation for the streamfunction. The advecting velocities are then interpolated back onto the nodes representing the PV contours in order to carry out the Lagrangian time-stepping of PV. The crucial technical issue resolved in [7] was the determination of an interpolation scheme linear in the number of nodes.

These developments have made the CASL algorithm competitive with spectral techniques for the study of rotating-stratified turbulence under the QG approximation and this has been exploited for horizontally periodic flows in [8,12]. (See [18,25,26], for spectral approaches on a fully periodic domain.) These ideas have been further developed to deal with flow on the surface of a sphere in [6].

It may seem at first sight that periodic boundary conditions are somewhat artificial and that they may not well represent flows in the presence of lateral boundaries. Of course laboratory experiments are necessarily performed in a confined domain, very often cylindrical (see, e.g. [1,4,22]). It is useful therefore to consider more realistic boundaries, and in particular that of a circular cylinder, arguably the simplest and most relevant boundary. This geometry is special also because it guarantees conservation of angular momentum, an important constraint of the fluid motion lacking in horizontally periodic geometry. Further, the geometrical constraint introduced by the presence of a boundary gives rise to a continued forcing

difficult to emulate in a periodic domain. Thus, for example, a vortex dipole in a cylinder will move linearly across the interior (in the absence of other interactions) until it reaches the cylinder wall, where it will split into opposite signed monopoles. These will then move around the inside of the boundary in opposite senses until they recombine and head off into the interior again. As the motion around the wall is relatively quick this gives a mechanism for significant mixing and enhanced interaction.

This paper describes the CASL algorithm for rotating stratified flow in a finite height circular cylinder. The treatment is 'inviscid' but with contour surgery employed to redistribute and in some cases ultimately remove filaments of small-scale of PV. It is known that viscous effects are significant in laboratory scale flows [15,17], particularly near the walls, but no attempt is made to model such effects here. Rather, our philosophy is that we are dealing with a crude model of an 'ocean basin', and weak topographic effects may be treated with an artificial layer of PV at the bottom of the domain, following [10] and references therein.

In future work we will extend the algorithm to deal with irregularly shaped lateral boundaries, allowing treatment of vortex trapping and shedding. In line with this, we have chosen to abandon the spectral approach in the radial direction (e.g. [23] following the ideas of [16]) and to employ instead a simple finite difference technique. This has the advantage that it encounters no difficulties with the coordinate singularity at the origin and also allows the use of a variable grid in radius, clustering points near the origin, that turns out to be useful for some applications. However, it is convenient to retain the Fourier treatment in azimuth. Further work on an irregular domain will probably revert to a Cartesian finite difference grid, i.e., abandoning all spectral techniques. This is, however, not inconsistent when one realises that spectral accuracy is lost when PV fields develop arbitrarily steep gradients through the largely unabated stretching of material contours (see e.g. [9,19]).

In the following section, the governing equations and their numerical treatment are presented. This is followed by the analysis of several simple though non-trivial test cases to check the convergence of the algorithm with increasing resolution and to illustrate the differences between the two radial grids used. We then move on to study a more complex flow, QG turbulence, and in particular focus on the differences between a cylindrical and a periodic domain. We find that the dependence on the initial total angular momentum is weaker than expected and that the various mechanisms for breakdown and merger of vortices previously found in other geometries also hold here, with little apparent change. Nor do the effects of boundary forcing lead to qualitative differences from what is found in periodic flows on the one hand or channel flows on the other. This follows because the cylinder radius is often large compared to a vortex radius, so that a dipole or monopole near the wall behaves locally rather as in a channel flow. Similarly, the fast redistribution of vortices allowed by the cylinder wall, discussed above, has an analogue in periodic flows, where a vortex leaves at one point on the boundary and 're-enters' at the corresponding periodic boundary location. In brief, the known conclusions for periodic flows are likely to be directly applicable, with the only differences arising from the presence of spurious image vortices.

2. Mathematical formulation

2.1. The governing equations

We consider flow in a cylinder of radius R and depth D, and work with cylindrical polar coordinates (r, θ, z), in terms of which the horizontal Cartesian coordinates are recovered by $x = r\cos\theta$ and $y = r\sin\theta$. The basic flow rotates about the cylindrical axis $r = 0$ at the rate $\Omega = f_0/2$, and the equations of motion are referred to a frame of reference rotating at this rate. Here, f_0 is the value of the Coriolis parameter $f(r)$ at $r = 0$, and we allow f to vary with r according to $f = f_0 - \gamma r^2$ to approximate the true variation of f near the pole on the Earth – this is the so-called 'gamma-plane' approximation. In all calculations in this paper we set $\gamma = 0$, but see [31] for an application of the current code with $\gamma \neq 0$ to the study of the polar

stratospheric vortex. The fluid is assumed to be stably stratified, so that the density $\rho(z)$ increases from the top to the bottom of the cylinder, and we have the buoyancy frequency $N(z)$ given by

$$[N(z)]^2 = -\frac{g}{\rho}\frac{\partial \rho}{\partial z}. \tag{1}$$

Throughout this paper we employ the *quasi-geostrophic approximation*, valid for small Rossby number Ro, where

$$Ro = \frac{U}{fL} \tag{2}$$

with L a characteristic scale in the horizontal, and U a characteristic horizontal velocity, and comparably small Froude number Fr, where

$$Fr = \frac{U}{NH} \tag{3}$$

with H a characteristic scale in the vertical. All three coordinates are scaled by the radius of the cylinder R so that $r = 1$ subsequently refers to the lateral boundary. This has no effect on the form of the equations. The dynamical evolution of the flow is governed by material conservation of PV, q, i.e.

$$\frac{\mathrm{D}q}{\mathrm{D}t} = 0 \tag{4}$$

or in polar coordinates, with u_r and u_θ the horizontal radial and azimuthal velocities, respectively,

$$\frac{\partial q}{\partial t} + u_r\frac{\partial q}{\partial r} + \frac{u_\theta}{r}\frac{\partial q}{\partial \theta} = 0. \tag{5}$$

The streamfunction ψ is determined by inversion of the generalised Poisson equation

$$\nabla_h^2\psi + \frac{\partial}{\partial z}\left(\left[\frac{f_0}{N(z)}\right]^2\frac{\partial \psi}{\partial z}\right) = q - f \tag{6}$$

with $\nabla_h^2\psi$ the relative vorticity, i.e., vorticity as observed in the rotating frame and ∇_h^2 the horizontal Laplacian. The radial and azimuthal velocity components u_r and u_θ are determined from the streamfunction using the non-divergent relations

$$u_r = -\frac{1}{r}\frac{\partial \psi}{\partial \theta}, \quad u_\theta = \frac{\partial \psi}{\partial r}. \tag{7}$$

At the top and bottom boundaries we impose the zero flux conditions

$$\frac{\partial \psi}{\partial z} = 0 \text{ at } z = 0, 1. \tag{8}$$

Small-amplitude bottom topography $z = \eta(x, y)$, necessarily with $|\eta| \ll D$, as is required for the quasi-geostrophic approximation, is incorporated via a fixed surface distribution of PV, say q_B at $z = 0$

$$q_B = -\frac{f_0}{D}\eta(x, y)\delta(z). \tag{9}$$

In practice, this delta-distribution of PV is approximated by a uniform distribution (in z) of PV in the bottom layer. It is often convenient to set up the initial PV so that there is *initially* no net PV perturbation

due to the topography, by adding a term initially equal and opposite to that in Eq. (9). However, this correction will in general evolve in time while the term q_B in Eq. (9) is fixed for all time.

2.2. Implementation of the CASL algorithm in a cylindrical domain

2.2.1. Overview

The functionality of the contour dynamics approach is provided with far greater efficiency in the CASL (contour-advective semi-Lagrangian) method [7] (henceforth DA97), but thus far only for the special case of horizontally periodic boundaries (or a channel). In this method a spectral approach is used to invert the Poisson equation (6) to find the velocities needed for the advection of the PV at each time-step according to Eq. (4). It is demonstrated in DA97 that only modest resolution is needed for the velocities with which the PV is advected (as opposed to the PV itself). This implies in turn that the streamfunction inversion can be carried out at moderate resolution. Accordingly, the crucial step in the development of their algorithm was the determination of an efficient technique for interpolating from the contour representation of q to a rectangular grid. These ideas have now been generalised in order to deal with problems on the surface of a sphere in [6]. It turns out that the approach needed for the cylindrical domain is very similar to that for the spherical surface, so that the code can be carried over to the new class of problems treated here with only minor changes.

In summary, the method works as follows. At each depth, the initial PV field is represented by contours, across each of which there is a specified jump in PV. Each of these contours is represented by a series of nodes. As time evolves, the nodes representing the PV contours will be advected by the prevailing velocity field, which in turn depends on the PV via the Poisson equation (6). If the nodes on a contour move apart significantly during the computation, extra nodes are inserted, to preserve accuracy in regions where the greatest changes take place. Conversely, the number of nodes may be reduced. This variable resolution is the powerful feature of the Lagrangian contour dynamics approach, but it is also its Achilles heel, as the filamentation of vorticity, and the corresponding generation of smaller and smaller scales, may give rise to an exponential growth in the number of nodes, all in the pursuit of PV features that are almost certainly not dynamically significant. This difficulty has in large measure been overcome by the use of *contour surgery* [5], where contours are broken or joined, and nodes removed or inserted, depending on local conditions, e.g., an extremely long thin filament of PV will be broken at its narrowest point thus forming two new filaments. This procedure limits the exponential growth in the number of nodes in problems where highly non-linear interactions are taking place, while numerical evidence accumulated over the last decade indicates that the corresponding numerical dissipation thus introduced is relatively minor.

The time-stepping of Eq. (4) uses a fourth-order Runge–Kutta scheme. The velocity field needed for the advection of PV is determined from the streamfunction, which in turn is found by inversion of the Poisson equation (6). The contour dynamics approach uses instead integrals over the PV to determine the velocity field: this can be computationally expensive since the cost increases with the *square* of the total number of nodes on the contours. By contrast, the CASL method of DA97 uses Eulerian techniques to determine the velocity field. This requires an additional step, namely the recovery of PV values on a regular grid. The critical step therefore in the CASL approach is the interpolation at each time-step from the highly accurate contour representation of PV onto a relatively coarse regular grid, with the number of operations proportional to the number of nodes on the PV contours. Accordingly, the velocity is also obtained on a relatively coarse grid. This is then interpolated back onto the irregular locations of the nodes in order to carry out the Lagrangian advection of PV. Thus the inherent assumption of the CASL algorithm is that the velocity field is required at significantly lower resolution than the PV field, but that the PV may still be accurately tracked in time. Calculations up to the present time have supported this assumption, which is made plausible by the fact that the spectral width of the velocity is much narrower than that of the PV, as is to be expected given that the PV is determined from velocity derivatives (see [18] and references therein).

We note that there are no depth derivatives in the (momentum) equation describing the advection of PV (4), by virtue of the quasi-geostrophic approximation. Thus when the PV is advected in the Runge–Kutta time-stepping scheme, each layer can be treated separately at each time-step. By contrast, the determination of the velocity field from Eq. (6) is fully 3-D and hence requires a fully 3-D solution technique.

2.2.2. Determination of the streamfunction

The method used for the determination of the velocity field at each time-step is almost exactly analogous to that used for a spherical surface in [6]. For brevity, that paper only describes the one-layer case, but the method follows through in an obvious way for the 3-D quasi-geostrophic problem and has indeed been programmed and used for such cases. We summarise the 3-D technique here, highlighting any modifications for cylindrical geometry.

Writing Eq. (6) explicitly in cylindrical coordinates and then multiplying through by r, we have

$$\frac{\partial}{\partial r}\left(\frac{r\partial\psi}{\partial r}\right)+\frac{1}{r}\frac{\partial^2\psi}{\partial\theta^2}+r\frac{\partial}{\partial z}\left(\left[\frac{f_0}{N(z)}\right]^2\frac{\partial\psi}{\partial z}\right)=r(q-f). \tag{10}$$

We now discretise the problem in (z,θ,r) (it is convenient to interchange the order of the coordinates r and z), with $z_i=i\Delta z,\ i=0,1,\ldots,N_z,\ \Delta z=D/N_z,\ \theta_j=j\Delta\theta,\ j=0,1,\ldots,N_\theta-1,\ \Delta\theta=2\pi/N_\theta$ and $r_k=k\Delta r$, $k=0,1,\ldots,N_r,\ \Delta r=1/N_r$, where N_z,N_θ and N_r are the numbers of grid-points in the three coordinate directions and where the grid is uniform in each of the coordinates (z,θ,r).

The first step is to decompose the fields into L normal modes in the vertical, so that

$$\psi(r,\theta,z;t)=\sum_l\psi_l(r,\theta;t)\chi_l(z). \tag{11}$$

Each mode is a solution of the Sturm–Liouville problem

$$\frac{\mathrm{d}}{\mathrm{d}z}\left(\left[\frac{f_0}{N(z)}\right]^2\frac{\mathrm{d}\chi_l}{\mathrm{d}z}\right)=-\lambda_l^2\chi_l \tag{12}$$

with zero flux conditions at $z=0,D$.

As in DA97, the Sturm–Liouville problem is set up in discrete form using second-order finite differences, and the eigenvalues $-\lambda_l^2,\quad l=1,\ldots,L$ and the discrete approximations to the vertical eigenmodes are calculated once and stored. We recommend choosing $L=N_z$ to resolve the often close dynamical coupling between small vertical and horizontal scales [12,30]. For constant N, as considered in the applications below, the vertical modes are cosine functions; however, the algorithm follows unchanged for more general $N(z)$.

Write the discrete form of (12) as

$$A_{i,l}\chi_l=-\lambda_l^2\chi_l, \tag{13}$$

$A=[A_{i,l}]$, and then $A=XDX^{-1}$ where the columns of X are the eigenvectors, and the elements of the diagonal matrix D are the eigenvalues. If now we take the discrete Fourier transform in the azimuthal direction in Eq. (10) then

$$\left[\frac{\mathrm{d}}{\mathrm{d}r}\left(r\frac{\mathrm{d}}{\mathrm{d}r}\right)-\left(\frac{m^2}{r}+r\lambda_l^2\right)\right]\hat{\psi}_{l,m}=\hat{\sigma}_{l,m} \tag{14}$$

with $\hat{\psi}$ the Fourier transform of ψ and $\hat{\sigma}$ the Fourier transform of $r(q-f)$ and where m is the azimuthal mode index, $m=-M/2,\ldots,M/2-1$ (with $M=N_\theta$ as FFTs are used to carry out the discrete Fourier

transform). Eq. (14) is equivalent to Eq. (2) of [6] for the spherical surface case, once our radial variable r is identified with $\cos\phi$ there (ϕ is latitude in the spherical surface problem).

Thus for each mode labelled (l,m) in the vertical and azimuthal directions, respectively, we have to solve the ODE in r as given in Eq. (14). This can be done using Chebyshev spectral techniques, as in [23], but that requires storage of the modal coefficients in r for each of the azimuthal modes (the inversion is too costly to carry out for every time-step) and in addition involves a non-uniform grid in r, which introduces extra difficulties in the interpolation procedures when switching between gridded and contoured PV. Accordingly, we have followed [6] and used a second-order finite difference discretisation in r on the uniform grid given above, with the tridiagonal inversion carried out at each time-step. Thus

$$\left(\frac{1}{\Delta r}\right)^2\left[r_{k+1/2}\left(\hat{\psi}_{l,m}^{(k+1)}-\hat{\psi}_{l,m}^{(k)}\right)-r_{k-1/2}\left(\hat{\psi}_{l,m}^{(k)}-\hat{\psi}_{l,m}^{(k-1)}\right)\right]-\left(\frac{m^2}{r_k}+r_k\lambda_l^2\right)\hat{\psi}_{l,m}^{(k)}=\hat{\sigma}_{l,m}^{(k)}, \tag{15}$$

where $r_{k+1/2}=(k+1/2)\Delta r$. The inversion of Eq. (15) must be carried out for each of the modes (l,m) whenever the velocity field is required (i.e., at each partial time-step in the Runge–Kutta procedure). In practice, the inversion takes most of the computational time. As the radial Eq. (15) is tridiagonal, the operation count for inversion is linear in the number of radial points. Thus for example, in a single layer case with 256 azimuthal points and 128 radial points, 100 time steps took approximately 13 s on a Compaq Alpha 600. Reducing the number of radial points by a factor of two halved the cpu time.

2.2.3. Treatment of the horizontal boundary conditions

For each radial inversion problem, conditions must be specified at the origin, $r=0$ and at the cylinder wall, $r=1$. We consider the simpler situation at $r=1$ first. The outer boundary condition is that there is no motion normal to the wall, i.e., $u_r=0$ at $r=1$ and hence, from (7) we find that $\psi=$ constant at $r=1$. Since the precise value of the constant is irrelevant (we are only concerned with the velocities (u_r,u_θ) which require horizontal derivatives of ψ) we set $\psi=0$ at $r=1$. Note that this formulation is essentially inviscid, so that there is in general a slip velocity tangential to the wall. There is also one other requirement at the cylinder wall. Nodes on the PV contours may be advected *through* the cylinder wall, due to non-zero radial velocities just inside the cylinder and the finite error of the time-stepping scheme; if this happens such nodes are brought back along the radial normal to the wall to $r=1-\varepsilon$, where $\varepsilon=\mathrm{O}(10^{-10})$.

We now turn to the boundary condition at $r=0$, i.e., at the coordinate singularity. This again has much in common with the treatment of the north and south poles in the spherical surface problem treated by [6]. We are interested in cases where the horizontal Cartesian velocities u and v are in general bounded and non-zero at the origin, i.e., $u\to u_0$ and $v\to v_0$ as $r\to 0$, where u_0, v_0 are constants (although the method also applies for cases where $u_0=v_0=0$). This implies that the angular momentum Γ must approach zero as $r\to 0$ since

$$\Gamma=ru_\theta=-ru\sin\theta+rv\cos\theta. \tag{16}$$

This condition can be used to determine a boundary condition for ψ at $r=0$ as follows, except in the special case of the barotropic mode, $\lambda_0=0$ (discussed below). From Eq. (16) $\partial\psi/\partial r=u_\theta$ is finite as $r\to 0$, while $\partial\psi/\partial\theta=-ru_r\to 0$. From these two relations, we can show that $\psi\to\psi^{(0)}=$ constant as $r\to 0$. Therefore we need a technique by which we can identify $\psi^{(0)}$. By performing a Taylor series expansion of Γ in r around the origin we can show that

$$\Gamma^{(0)}=\frac{3\Gamma^{(1/2)}-\Gamma^{(3/2)}}{2}+\mathrm{O}((\Delta r)^2), \tag{17}$$

where $\Gamma^{(0)}$ is the angular momentum at the origin and $\Gamma^{(1/2)}=\Gamma(\Delta r/2)$, etc. Now $\Gamma^{(0)}$ is required to be zero, and we can rewrite Eq. (17) in terms of the discrete Fourier transform of the streamfunction, noting that as

$r \to 0$ all azimuthal modes except that for $m = 0$ must tend to zero, since $\psi = \psi^{(0)}$ at the origin. Hence we find

$$\hat{\psi}^{(0)}_{l,m} = 2\hat{\psi}^{(1)}_{l,m} - \hat{\psi}^{(2)}_{l,m} + \mathrm{O}((\Delta r)^2), \quad m = 0. \tag{18}$$

Thus we have a boundary condition for $\hat{\psi}^{(0)}_{l,0}$, which corresponds to that given in [6] for the spherical surface case, once we identify r with $\cos\phi$, as before. For the modes $m \neq 0$, as noted above, we have $\hat{\psi}^{(0)}_{l,m} = 0$.

Finally, for the barotropic mode (which has $\lambda_0 = 0$), a tridiagonal inversion is not required for $m = 0$, as in this special case the Poisson equation (6) can be integrated once in r by numerical quadrature (using the trapezoidal rule for second-order accuracy), thus giving $\hat{\Gamma}^{(k)}_{0,0}$ which in fact is all we require, as described below.

2.2.4. Determination of the Cartesian velocities u and v

In practice once ψ is known, we can find u and v from

$$u = -\frac{\Gamma y + xw}{r^2}, \quad v = \frac{\Gamma x - yw}{r^2}, \tag{19}$$

where $w = \partial\psi/\partial\theta$, the transform of which is immediately obtained from $\hat{\psi}$ by multiplying by im. It is convenient to rewrite Eq. (19) in the form

$$u = -\frac{\Gamma}{r}\sin\theta - \frac{w}{r}\cos\theta, \quad v = \frac{\Gamma}{r}\cos\theta - \frac{w}{r}\sin\theta. \tag{20}$$

The fields of Γ/r and w/r are available at all grid points; at the origin, they are found by cubic extrapolation in r, i.e.

$$\left(\frac{\Gamma}{r}\right)^{(0)} = 3\left(\frac{\Gamma}{r}\right)^{(1)} - 3\left(\frac{\Gamma}{r}\right)^{(2)} + \left(\frac{\Gamma}{r}\right)^{(3)} + \mathrm{O}((\Delta r)^3)$$

for each discrete angle $\theta = \theta_j$. At the outer boundary $w = 0$ and Γ/r is found by quadratic extrapolation in r. This permits one to evaluate u and v at any point within the cylinder, including at $r = 0$, where u and v are independent of θ. For the PV advection, the velocity is required at the contour nodes, and this is obtained from a bi-linear interpolation in r and in θ of the gridded fields Γ/r and w/r.

3. Results

We first describe a few simple tests, to confirm that the cylindrical CASL code produces expected results. We then consider some cases in which the forcing introduced by the presence of the cylindrical wall introduces interesting phenomena, following [8] who considered the horizontally periodic case, using initially random distributions of positive and negative columnar vortices to study quasi-geostrophic turbulence, but now in addition exploring the effects of non-zero net angular momentum.

An idealised problem in cylindrical geometry that can be treated analytically is the inviscid problem of the motion of a 2-D point vortex within a circular region, with the boundary condition of zero radial velocity at the circular boundary. If a point vortex of strength κ (equal to the circulation divided by 2π) is located at radius $r = \alpha$ then its motion is determined by the velocity field induced by the image vortex located at the inverse point $r = 1/\alpha$ (see e.g. [29]). The corresponding velocity has magnitude

$$v = \kappa\frac{\alpha}{1-\alpha^2} \tag{21}$$

and acts in the θ direction, i.e., anti-clockwise for κ positive. Therefore the point vortex moves in a circle of constant radius α with $\mathrm{d}\theta/\mathrm{d}t = v/\alpha$. The 2-D point vortex result can also be used to approximate the problem of the motion of a single column of uniform PV (i.e., modelled by a single circular contour of radius say a and centre at radius α in each layer) the upper and lower rigid boundary conditions can be treated by using the method of images in the vertical, so that we once again have a vortex of infinite extent, and the vortex patch at each vertical level is taken as equivalent to a point vortex of strength $a^2 q_0/2$ where q_0 is the (uniform) PV of the patch.

The point vortex model is compared with some single layer CASL runs in Fig. 1 (multi-layer runs give identical results). In the figure, time is scaled so that the vortex rotation time is unity in each case. The mean location of the vortex contour was calculated at each time point (significant distortion of the patch was evident in some runs, particularly those where the patch had its centre near the cylinder wall) and then the time-averaged value of $\mathrm{d}\theta/\mathrm{d}t$ for the centre of PV was determined for comparison with the theoretical value. The agreement is in general surprisingly good, even for cases where the centre of PV deviated from a constant radius.

For vortex patches located close to the centre of the cylinder, numerical calculations showed the patch rotating in the opposite sense to that predicted by the point vortex model. This was the case for $a = 0.1, \alpha = 0.1$ for example. However, this behaviour turns out to be grid-dependent and incorrect, but not resolvable with the standard model: the results shown in the figure were obtained for small α using the following alternative version of the code. (Even with this improved approach, as many as 1028 radial points were needed to obtain good accuracy for small α.) The modified version uses a radially variable grid spacing in r, based on a grid uniform in s, where $r = s^2$. This clusters radial grid points near the origin and might therefore be thought to lead to difficulties with numerical instability because of the coordinate singularity. However, in practice no problems were encountered and it was found that for more general problems (e.g.,

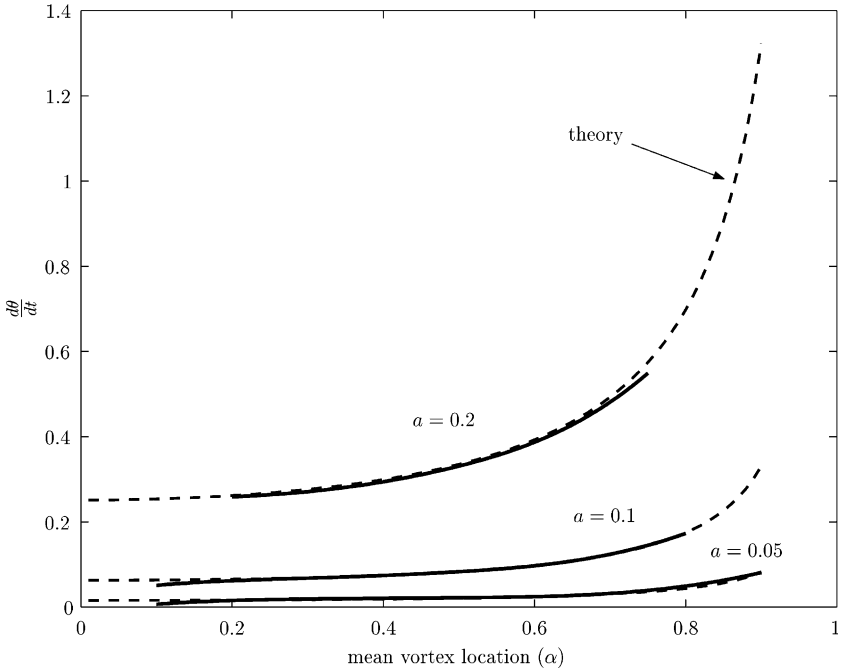

Fig. 1. Comparison of the rotation rate for a single circular patch of PV $q = 2\pi$, radius $a = 0.2, 0.1$ and 0.05, centred initially at $(0, \alpha)$, shown as full curves, compared with the analytical solution for an equivalent point vortex, i.e., $\mathrm{d}\theta/\mathrm{d}t = \pi a^2/(1 - \alpha^2)$, shown dashed.

stratified turbulence calculations) that the two radial grids gave effectively identical results. For the majority of cases treated in this paper, where vortices are close to uniformly distributed over the domain, the uniform radial grid is probably preferable (for the same number of radial grid points, the uniform grid gives twice the resolution at the cylinder boundary). By contrast, problems such as study of the polar vortex [31] where one wishes to simulate a large domain, but focus on the dynamics near the origin and far from the influence of the boundary are best treated with the variable radial grid. For such problems a cylindrical domain with the boundary well removed from the origin is more natural than a periodic domain.

The implementation of a variable radial grid is particularly straightforward in CASL: all that is required is to transform the Poisson equation for the streamfunction to s, θ coordinates, so that the 'radial' coordinate spacing remains uniform (in s) for this part of the algorithm. The contour to grid conversion of PV, required to determine the right-hand side of the Poisson equation before inversion, is performed using the s, θ coordinates, but with no coding changes. The Poisson equation is then inverted on a uniform s grid and finally the advecting velocities for the PV field are determined by interpolation as usual. For programming convenience, all further advection calculations are then performed in Cartesian coordinates.

Returning to Fig. 1, it can be seen that the high resolution near the origin attainable with the variable radial grid model allows good agreement with the point vortex result, but that accuracy still degrades as the vortex patch is made smaller and/or taken closer to the centre.

A simple analytical model can also be constructed to check cases where there is depth dependence, i.e., fully 3-D behaviour. We consider the case where a column of uniform PV $q = q_0$ extends over the range $\tilde{z} \in [\pi/4(1-\beta), \pi/4(1+\beta)]$, where $\tilde{z} \equiv Nz/f_0$ is a stretched vertical coordinate (in terms of which the left-hand side of (6) becomes simply the 3-D Laplacian), and where the total scaled depth $ND/f_0 = \pi/2$. Generalising the point vortex model to this case gives as the image a line vortex at $r = 1/\alpha$ with discrete segments of PV q_0 and of scaled height $\beta\pi/2$ corresponding to the original vortex and an infinity of periodic images in depth.

Therefore, the induced velocity is

$$v = \sum_{j=-\infty}^{\infty} \kappa \frac{\alpha}{1-\alpha^2} \left(\cos\theta_j^1 + \cos\theta_j^2 \right), \tag{22}$$

where θ_j^1, θ_j^2 are the angles at the base of the triangle constructed by joining the two ends of the jth segment of the image vortex to the centre of PV of the original vortex blob (see Fig. 2). This is the result of [29, p. 172] for a line segment of vorticity but summed over the images in the vertical. This formula was summed numerically (101 terms were used) and the results are displayed in Fig. 3 as solid curves for two cases, one where the vortex column is extending through the full depth with PV $q = q_0 = 8\pi$, and the other where only the middle half has non-zero PV $q = q_0$, having $\beta = 1$ and $\beta = 0.5$, respectively. In each case the vortex radius $a = 0.14$. Also shown as the dashed curve on the figure is the case $\beta = 1$, i.e., a uniform column, but with $q = q_0/2$. We see that the half-fill case ($\beta = 1/2$) approaches the case $\beta = 1, q_0$ as $\alpha \to 1$, i.e., as the column of PV approaches the cylindrical boundary, and that for small α it approaches the $\beta = 1, q_0/2$ case. Physically, this corresponds to the fact that as the observation point approaches the image vortex, i.e., as $\alpha \to 1$, the local strength of the vortex determines the velocity field, whereas as $\alpha \to 0$, the velocity induced corresponds to an infinite line vortex, but with half the strength, i.e., the average of the non-zero and zero valued segments. The roll-off in the cases for $\beta < 1$ near the centre of the cylinder ($\alpha = 0$) is present because of the finite number of terms taken in the sum. To compare with this model, the CASL code was used with an initial condition given by a column of PV, with radius $a = 0.14$ and centre $\alpha = 0.8$ but with depth-dependent PV. The scaled depth was $\pi/2$ and 28 layers were used in the vertical. In the top six layers the vortex had $q = q_0 = 8\pi$, in the middle 15 layers the PV was set to zero, and then in the bottom 7 layers the PV was $q = q_0/10$. The vortex in the top layer (with $q = 8\pi$) rotated with an average $\mathrm{d}\theta/\mathrm{d}t = 0.205$, compared with the theoretical point vortex value of 0.207, whereas the vortex in the bottom layer had

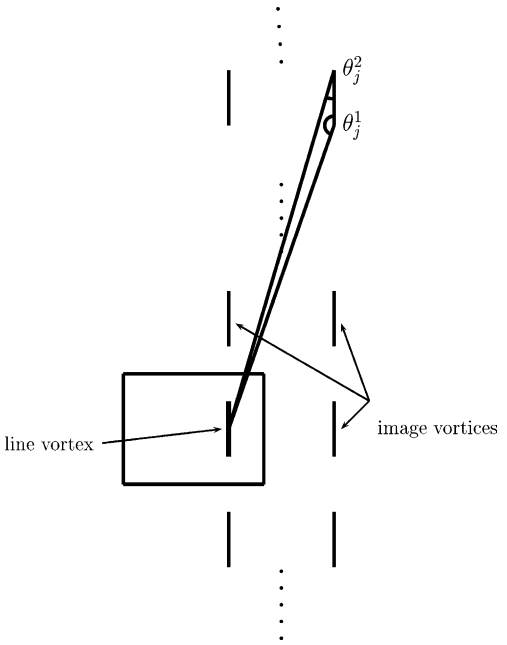

Fig. 2. Schematic of a line vortex in the cylinder with the corresponding image vortices in the horizontal and vertical and the associated angles θ_j^1 and θ_j^2.

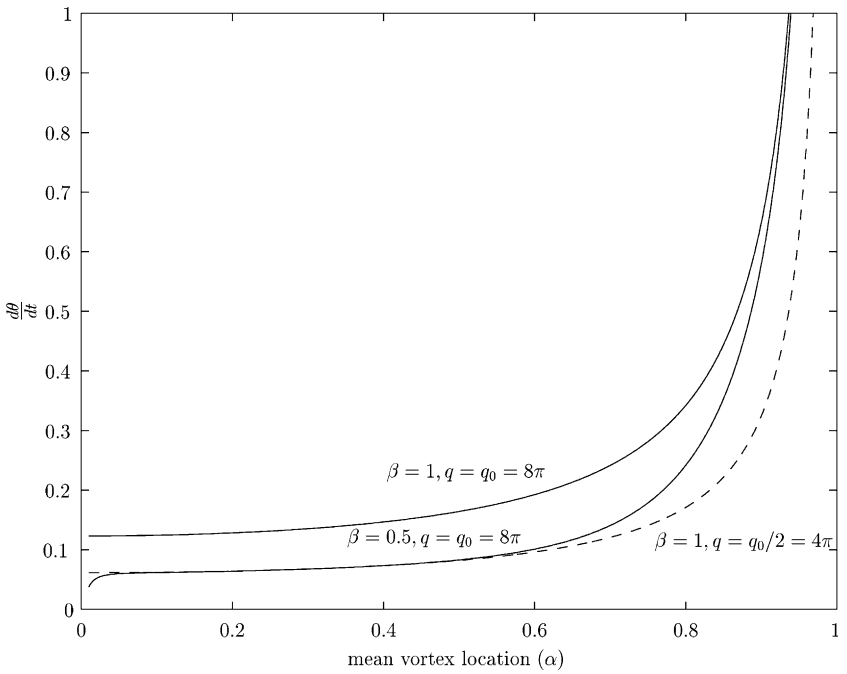

Fig. 3. Analytical approximation for the rotation rate of a full-depth circular column of PV $q = q_0 = 8\pi$ ($\beta = 1$), and a centred half-depth column ($\beta = 0.5$), plotted as a function of the radial location of the centre (α). Both these cases are shown as full curves, while the dashed curve shows a full-depth column (i.e., $\beta = 1$) with $q = 4\pi$. In all cases the column has radius $a = 0.14$.

$d\theta/dt = 0.0227$ which agreed with the theory to that number of decimal places. Increasing the PV in the bottom 7 layers to $q_0/2 = 4\pi$ gave a numerical result of 0.112 compared with the theoretical result of 0.114.

A further 2-D test of the code, which assesses the treatment at the origin and at the cylinder boundary, is given by the special case where $q = 2\pi$ in the left semi-circular half of the cylinder and -2π in the right half. The streamfunction can be found exactly in this case (see Appendix A, Eq. (A.10)) and in addition, the y component of the velocity at the origin takes the value $v = 8/3$, which can be shown directly from Eq. (A.1), using the expression valid on the y-axis, $v = -(1/r)(\partial\psi/\partial\theta)$ and then taking the limit $r \to 0$.

In Table 1, we show how the maximum error varies with the number of grid points, for both the fixed radial grid and the variable radial grid codes. As expected, the maximum absolute error is approximately $O((\Delta r)^2)$ for both versions of the code. Also shown is the numerically determined value of the velocity at the centre, which agrees well with the analytical value of $v = 8/3$.

We now move on to compare 2-D simulations for the circular domain with those for a periodic domain, both conducted using the CASL method. The initial condition consists of a single positive vortex patch of magnitude 2π and radius 0.2, with a second negative patch whose centre is located 0.5 units from the centre of the circle. We allow the ratio σ of the PV magnitudes of the negative to the positive patches to vary from 0 to 1. One extreme is the case $\sigma = 0$, where the off-centre patch plays the role of a passive marker. One expects very similar behaviour for the doubly periodic and circular domains, because the location of the central patch remains fixed for all time in both cases, and the other 'patch' is swept around the central vortex into an extended spiral filament in both cases, reflecting the circular symmetry of the velocity field generated outside the central vortex by the central vortex. In this case the periodic results are very close to those for an infinite domain, as the vortex radius is small compared to the box length of 2π. The two codes produce very similar results for values of σ between 0 and about 0.3. Thus, for example, when $\sigma = 0.25$, the outer (weak) patch rotates around the strong central patch, with filamentation of the outer patch followed at long times by the somewhat diminished outer patch rotating around the essentially unchanged inner strong patch. Only the details of the filamentation vary in the two calculations.

However, as σ is increased in magnitude, the two calculations differ markedly. This can be understood in the case $\sigma = 1$, where in the periodic case the resultant dipole propagates in a straight line, repeatedly crossing the periodic boundary. By contrast, for the circular domain, the dipole propagates until it reaches the boundary, splits into two monopoles which travel around the boundary in opposite directions until they meet and reform as a dipole. This process repeats, typically with a weak precession. The behaviour for an intermediate value of $\sigma = 0.4$, say, reflects this essential difference between the two domains. As we can see in Figs. 4 and 5, the initial behaviour is very similar in both cases. However, as time progresses, in the case of the circular domain, the outermost (weak) patch reaches the wall and then travels around the wall in the opposite sense to the corresponding patch in the periodic case. Clearly the 'image patch' is locally dominant at this stage, and we note enhanced filamentation and deformation of the weak patch in the circular domain. This generic behaviour is repeated over time, leading to a diffuse distribution of negative PV

Table 1
Dependence of truncation error on grid size

N_θ	N_r	Radial grid	|Max. error|	$v(0,0)$
128	64	Variable	8.36×10^{-4}	2.6613
256	128	Variable	2.43×10^{-4}	2.6652
512	256	Variable	6.72×10^{-5}	2.6663
1024	512	Variable	1.80×10^{-5}	2.6666
128	64	Fixed	7.97×10^{-4}	2.6661
256	128	Fixed	2.35×10^{-4}	2.6665
512	256	Fixed	6.58×10^{-5}	2.6666
1024	512	Fixed	1.78×10^{-5}	2.6667

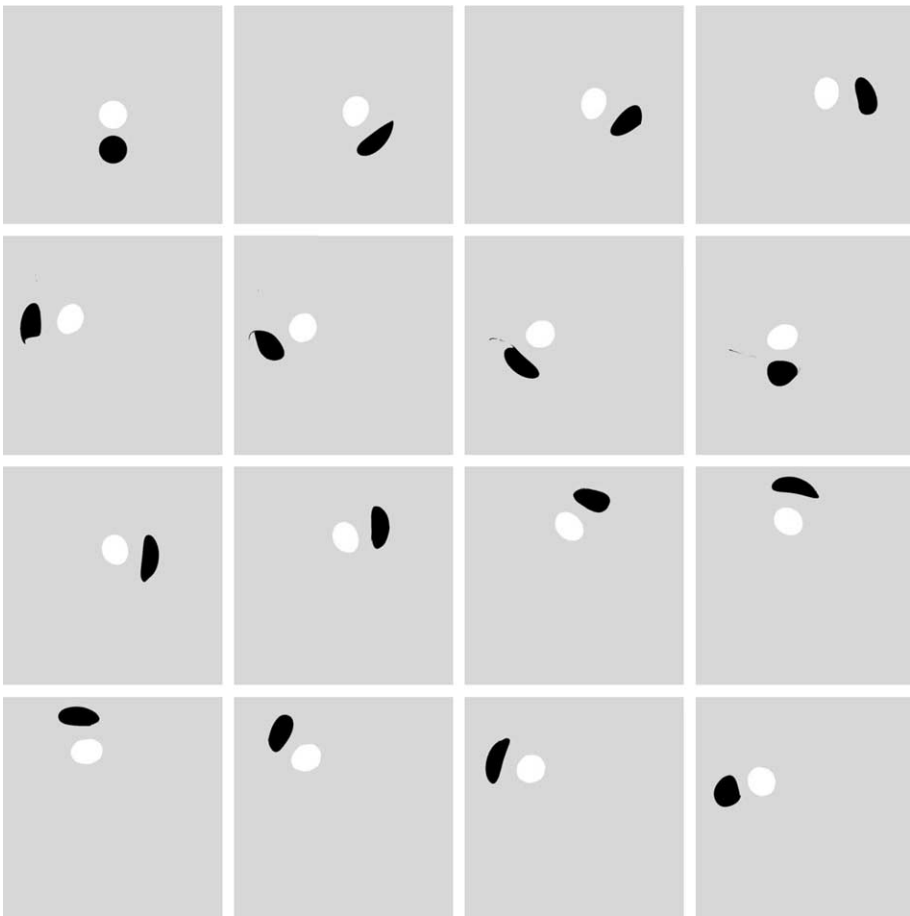

Fig. 4. Doubly periodic 2-D simulation of two circular vortex patches, with radius 0.2 and with $q = 2\pi$ (the central white patch in the first frame), and $q = -0.8\pi$ (the dark patch in the first frame), so that $\sigma = 0.4$. The frames run in time from left to right, and then from top to bottom, for times $t = 0, 2, 4, 6, 20, 22, 24, 26, 100, 102, 104, 106, 200, 202, 204, 206$. Here a vortex circulation time is 2 time units for the original positive patch. Only the central quarter of the domain is shown.

surrounding an essentially unchanged positive vortex patch. By contrast, for the periodic case, after some initial breakup and filamentation of the weaker negative patch of PV, a state where the negative patch orbits the central positive patch is quickly established. Thus, dependent on initial conditions, and especially when there is a dominant monopole present, there is a tendency for PV of one sign to be broken down in the circular domain.

These observations have some bearing on the role of angular momentum in 2-D stratified turbulence, a topic that was studied numerically in a circular domain in [21]. In [21] it was demonstrated that initially random distributions of PV evolve into one of two alternative final states: either a dipole, which is found when the total angular momentum is zero, or a monopole, typically surrounded by diffuse PV of the opposite sign, which is found for non-zero total angular momentum. The calculations of [21] included the effects of viscosity and were carried out for both non-slip and stress-free boundary conditions, the latter being closer to the free-slip case studied here. As is pointed out in [21] in the stress-free case it is possible to adjust the rotation rate so as to set the total angular momentum to zero whereas this is not possible for the no-slip case. Thus, it is expected that simulations with the stress-free boundary condition should always

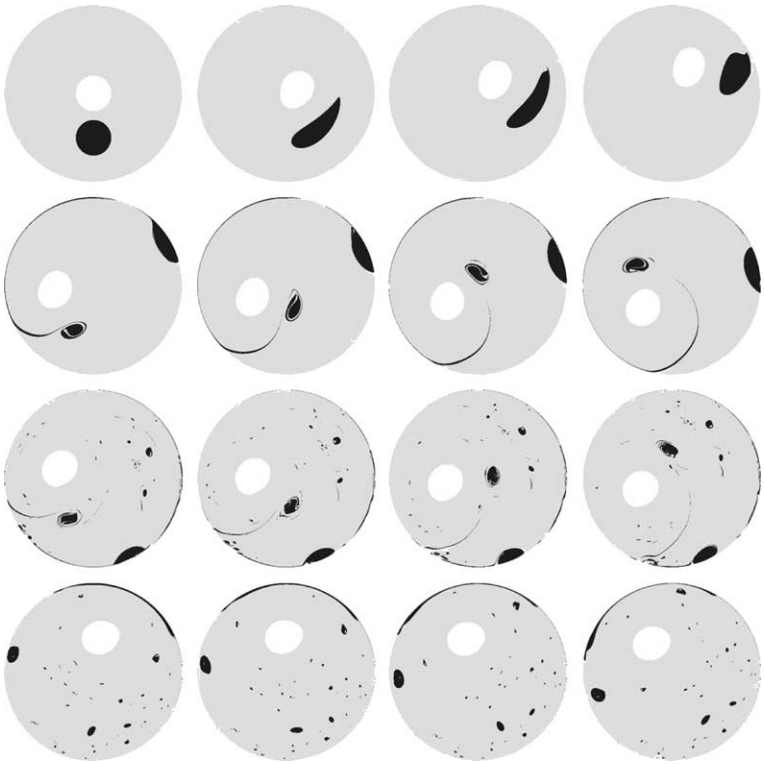

Fig. 5. Cylindrical 2-D simulation of two circular vortex patches, with radius 0.2 and with $q = 2\pi$ (the central white patch in the first frame), and $q = -0.8\pi$ (the dark patch in the first frame) so that $\sigma = 0.4$. The frames run in time from left to right, and then from top to bottom, for the same times shown in the previous figure.

evolve to a final state corresponding to the zero total angular momentum case. This was confirmed in practice with only the dipolar final state achievable for the stress-free boundary condition, whereas by adjusting the initial angular momentum either final state could be found for the no-slip boundary. The laboratory work of [24] in a circular tank, necessarily satisfying a no-slip condition at the tank wall, found similar dependence of the final state on the total angular momentum introduced initially.

Our calculations also support these findings. Thus if we take an initial randomly located distribution of vortex patches, with zero total circulation, we find that the final state is a dipole, irrespective of the initial total angular momentum, which can be adjusted by weighting the distribution of vortex patch locations so that more of the vortices of one sign are clustered near the centre of the domain. This is in agreement with the calculations employing stress-free boundary conditions described in [21]. However, our discussion of the two patch problem above indicates that by adjusting the initial distribution of PV, a final state closer to a monopolar patch surrounded by PV of the opposite sign might be achieved. In Fig. 6, accordingly, we show a distribution of vortex patches where the positive patches all have $q = 4\pi$ and the negative patches all have $q = -1.2\pi$, i.e., $\sigma = 0.3$. However, both negative and positive patches are uniformly distributed over the circular domain, so that the total angular momentum is positive. The final state shows a strong central patch of positive PV, surrounded by diffuse negative PV. This is clearly not the same as the extremely well defined, centrally located monopole found in Fig. 6 of [21], but there are definite similarities, indicating that not only the total angular momentum, but also, and perhaps more importantly, the nature of the distribution of PV determines the nature of the final state encountered.

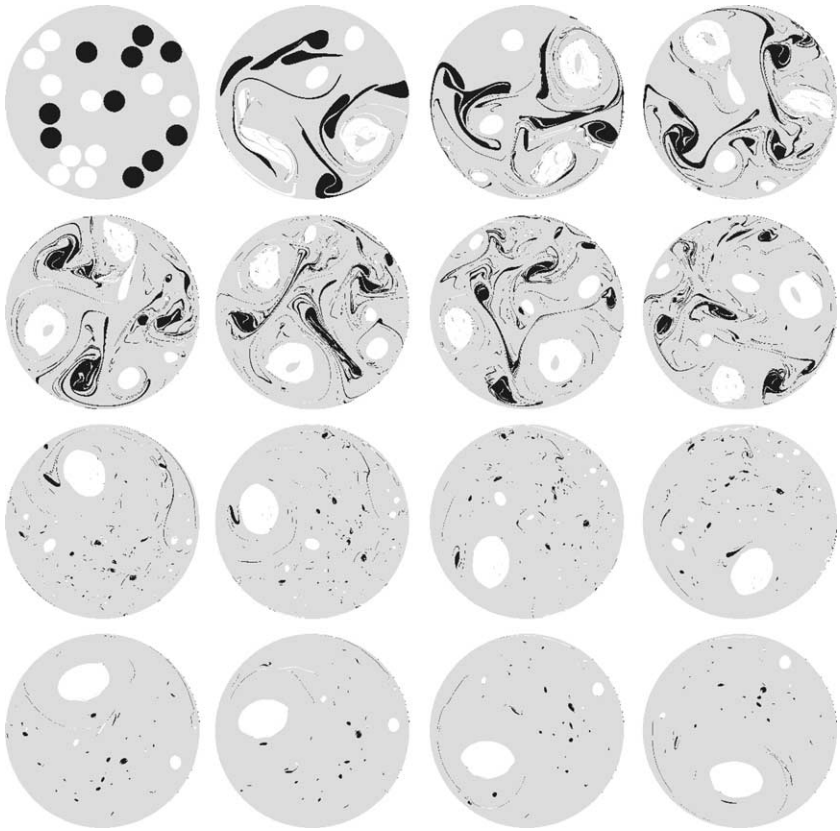

Fig. 6. Cylindrical 2-D simulation of 20 circular vortex patches, filling a quarter of the cylinder, with $q = 4\pi$ (the 10 white patches in the first frame), and $q = -1.2\pi$ (the 10 dark patches in the first frame) so that $\sigma = 0.3$. The frames run in time from left to right, and then from top to bottom, for times $t = 0, 2, 4, 6, 8, 10, 12, 14, 40, 42, 44, 46, 80, 82, 84, 86$. Here a vortex circulation time is 1 time unit for the original positive patches.

A variety of 3-D simulations have been conducted as well to examine the role of the boundary conditions and the angular momentum. Consider first a case having no net circulation nor angular momentum. Initially, the vortices are columnar (2-D) except for the addition of small random 3-D perturbations, and are located randomly within the domain, as in the 2-D examples above. There are 25 vortices of each sign ($q = \pm 4\pi$) altogether occupying one-eighth of the domain volume – this gives a vortex diameter of 0.1. The scaled depth of the domain is 0.4, so that each vortex has a height-to-width aspect ratio of 4, and the depth is divided into 20 layers.

In the periodic case, such vortices are known to break down into 3-D vortices, mainly domes at the upper and lower surfaces [8]. Fig. 7 shows the flow evolution in the present case. Qualitatively, the evolution is similar to the periodic case with the formation of two or three significant domes of each sign of PV attached to each surface. There are a few important differences, as seen for example in the rapid attrition of the positive vortex lying against the domain wall in the upper right-hand part of the figure from $t = 50$ to 60. This is caused by the strong interaction with its image vortex, and at $t = 60$ one can see long streamers in the wake (to the right) of this ''vortex pair''. By $t = 70$, whatever is left of this vortex is captured by another larger like-signed vortex at the upper surface (which at $t = 60$ was itself moving rapidly counter-clockwise along the right-hand side of the domain wall). Another example of rapid vortex propagation

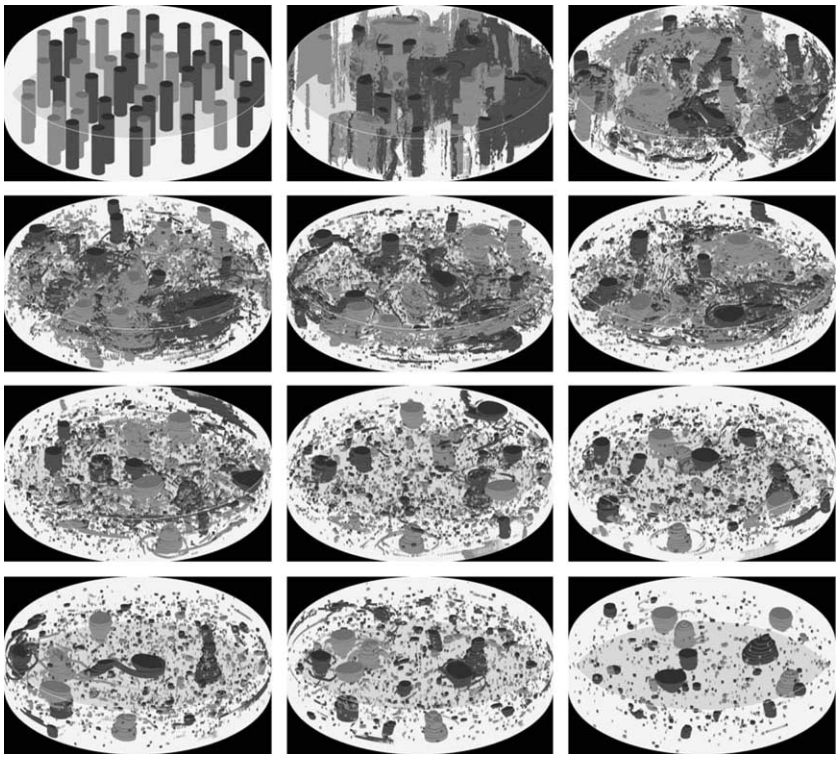

Fig. 7. Cylindrical 3-D simulation of 25 circular columnar vortices of each sign ($q = \pm 4\pi$) and with radius 0.1, so filling one eighth of the volume of cylinder. The frames run in time from left to right, and then from top to bottom, for times $t = 0, 10, 20, \ldots, 90, 100, 200$. Columns of negative PV have lighter shading in the first frame. The vortices are uniformly distributed so that the total angular momentum is zero.

along the domain wall is seen between $t = 80$ and 90, as a negative PV dome moves clockwise around the front wall of the domain. Shortly after $t = 90$, this dome runs into a positive PV dome and both vortices leave the domain wall as a dipole.

This case is next contrasted by another which differs only in the way in which the positive and negative vortex columns are initially positioned. In order to set up an angular momentum variation (a radial variation in the azimuthal mean value of Γ), a probability function $P(r) = r^2$ and its complement $1 - P(r)$ are used to position the positive and negative columns, respectively. This places more negative columns near the centre of the domain, and more positive ones near the outer wall. All other parameters (vortex size, depth, etc.) are the same as in the previous case. Fig. 8 shows the flow evolution in the same format as in Fig. 7 to allow comparison. At early times in the present case, the negative columns rapidly condense into large domes at the upper and lower surfaces, which remain near the domain centre for all times, while the positive columns break down into significantly smaller domes and generally fragment by image dipolar interactions at the domain wall. The final state shown broadly retains the initial variation in angular momentum, and does not yet show the formation of a single dipole as in the 2-D examples. Here, such a dipole may never form since the vortices interact less vigorously in 3-D (the flow field decays like the inverse-squared distance from a vortex, in contrast to the inverse distance decay in 2-D). Moreover, the strong interactions that occurred during the initial break down of the vortex columns has left the middle fluid layers largely depleted of PV, and so any final state must be fundamentally 3-D.

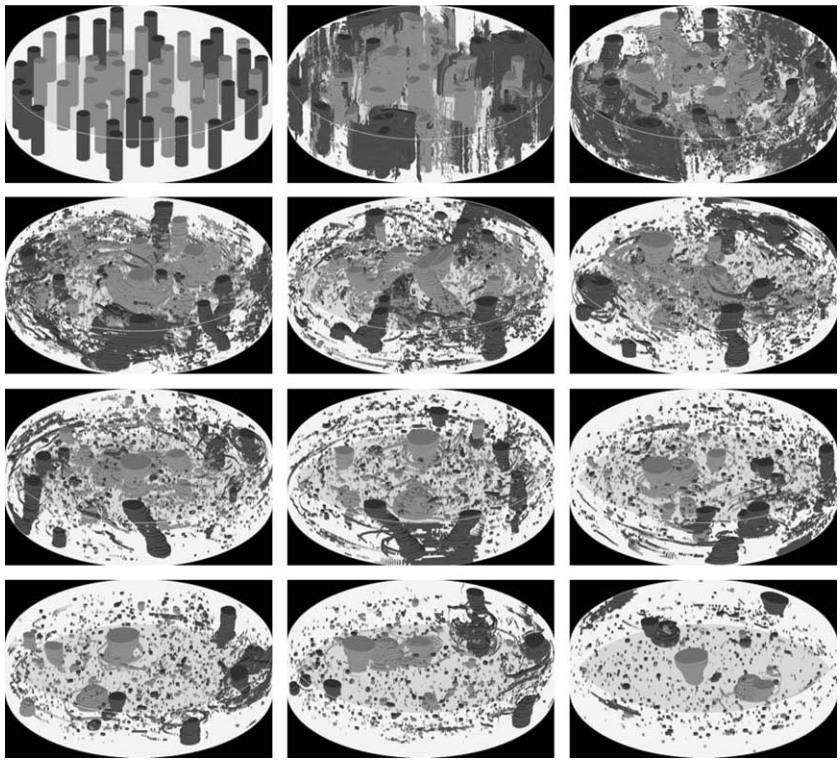

Fig. 8. Cylindrical 3-D simulation with vortex parameters as in the previous figure, but with a different initial distribution of vortex columns, with the negative columns (lighter shading) clustered near the centre of the domain, so that there is a radial distribution of azimuthally averaged angular momentum. The frames run from left to right, and then from top to bottom, with the same times as in the previous figure.

4. Summary and outlook

In this paper, we have outlined the extension of the CASL algorithm for the study of rotating, stratified quasi-geostrophic flows in a cylindrical domain. Test cases verify that the spatial accuracy of the method is second-order in the mean grid size, consistent with the second-order discretisation used in the radial and vertical directions. It is noteworthy that the CASL algorithm is better suited to studying nearly inviscid flows, characterised by a extensive range of active vortical structures, than more conventional grid-based or spectral-based algorithms, first because of the Lagrangian treatment of potential vorticity advection, and second because much larger time steps can be used in CASL while maintaining solution accuracy.

These advantages of the CASL algorithm are not restricted to quasi-geostrophic flow in simple geometries. The CASL algorithm has also been implemented in more realistic flows (e.g., shallow water and Boussinesq, valid for order unity Rossby and Froude numbers) with similar success [9,13,32]. The above applications have so far used only periodic horizontal boundary conditions. The current work demonstrates the viability of modelling horizontally bounded flows, and it is the first step towards modelling flows in arbitrary domains, for any set of equations for which accurate potential vorticity conservation is required. However, for problems where viscosity plays a significant role, such as laboratory experiments in relatively small tanks, the present approach, which uses a slip boundary condition at the wall, is not appropriate.

For arbitrary domains, the spectral approach used here in part is no longer viable. We are currently developing new methods that maintain second-order accuracy for the flow field in such domains. These methods return to the simplicity of a rectangular (or square) grid. However, the tridiagonal matrix approach in radius must also be abandoned and a pentadiagonal matrix problem must be solved in the horizontal, resulting in a time penalty compared with the methods used in the present paper. The interface with contour dynamics remains straightforward: one can still recover the potential vorticity field on the grid using the technique originally developed in [7], with only slight modifications, and the advection step, that of integrating $\mathrm{d}x/\mathrm{d}t = u$ and $\mathrm{d}y/\mathrm{d}t = v$ for the points on the contours requires no modification at all. In comparison with classical finite difference QG codes, these techniques should provide improved accuracy for the PV, due to the Lagrangian approach used for the advection of PV. The cost of calculating the streamfunction (and hence the velocity field needed for the advection of PV contours), will be equivalent to that of classical finite-difference methods, with the major advantage that only a relatively coarse grid is required and that larger time steps may be taken without introducing numerical instability. We hope to report on this extension in the near future.

Acknowledgements

DGD is grateful for the support of Sydney University during two visits to develop this and related research in collaboration with CM. This work was partly supported by the Australian Research Council.

Appendix A

Here we provide a short derivation for the form of the 2-D streamfunction ψ satisfying $\nabla^2\psi = \pm 2\pi$ in the left and right semi-circular domains corresponding to the left and right halves of the cylinder. We begin with the superposition of elementary solutions

$$\psi = 2\pi \sum_{m \text{ odd}} \frac{1}{m} \bar{\psi}_m(r) \cos m\theta (-1)^{(m-1)/2} \tag{A.1}$$

with

$$\bar{\psi}_m(r) = \frac{4}{\pi} \frac{r^2 - r^m}{m^2 - 4} \tag{A.2}$$

which satisfies the boundary condition $\psi = 0$ at $r = 1$. In addition

$$\nabla^2(\bar{\psi}_m(r) \cos m\theta) = -\frac{4}{\pi} \cos m\theta \tag{A.3}$$

for each m, and so

$$\nabla^2\psi = -8 \sum_{m \text{ odd}} \frac{1}{m} \cos m\theta (-1)^{(m-1)/2} = -2\pi \operatorname{sgn}(\cos\theta) \tag{A.4}$$

as required. The solution in Eq. (A.1) is unwieldy however, because of the infinite sum involved, but this sum can actually be obtained explicitly, as we now demonstrate. We can rewrite Eq. (A.1) in the form

$$\psi = 2\pi \mathrm{i}\left[S(r\mathrm{e}^{\mathrm{i}(\theta+\pi/2)}) + S(r\mathrm{e}^{-\mathrm{i}(\theta-\pi/2)}) - r^2 S(\mathrm{e}^{\mathrm{i}(\theta+\pi/2)}) - r^2 S(\mathrm{e}^{-\mathrm{i}(\theta-\pi/2)})\right], \tag{A.5}$$

where

$$S(a) = \frac{2}{\pi} \sum_{m \text{ odd}} \frac{a^m}{m(m^2-4)}. \tag{A.6}$$

If we break Eq. (A.6) into three parts using partial fractions, then the derivative of each individual sum with respect to a can be expressed in terms of

$$S_0 = \sum_{m \text{ odd}} a^m = \frac{a}{1-a^2} \tag{A.7}$$

by suitably multiplying or dividing by powers of a. Integrating with respect to a we find

$$S(a) = \frac{1}{4\pi}\left[-\left(a + \frac{1}{a}\right) + \left(a - \frac{1}{a}\right)^2 L(a)\right], \tag{A.8}$$

where

$$L(a) = \int_0^a \frac{1}{1-a^2}\,\mathrm{d}a = \frac{1}{2}\ln\left|\frac{1+a}{1-a}\right|. \tag{A.9}$$

Thus the final form for ψ is

$$\begin{aligned}\psi = {} & (r - r^{-1})\cos\theta + \frac{1}{4}(r^2 - r^{-2})\sin 2\theta \ln\frac{1 + r^2 - 2r\sin\theta}{1 + r^2 + 2r\sin\theta} \\ & + \frac{1}{2}\left[2 + (r^2 + r^{-2})\cos 2\theta\right]\tan^{-1}\left(\frac{2r\cos\theta}{1-r^2}\right) - \pi r^2 \cos^2\theta\,\mathrm{sgn}(\cos\theta).\end{aligned} \tag{A.10}$$

References

[1] B.M. Boubnov, S.B. Dalziel, P.F. Linden, Source-sink turbulence in a stratified fluid, J. Fluid Mech. 261 (1994) 273–303.
[2] X. Carton, Hydrodynamical modeling of oceanic vortices, Surv. Geophys. 22 (2001) 179–263.
[3] J.G. Charney, M.E. Stern, On the stability of internal baroclinic jets in a rotating atmosphere, J. Atmos. Sci. 19 (1962) 159–172.
[4] F. de Rooij, P.F. Linden, S.B. Dalziel, Experimental investigations of quasi-two-dimensional vortices in a stratified fluid with source–sink forcing, J. Fluid Mech. 383 (1999) 249–283.
[5] D.G. Dritschel, Contour dynamics and contour surgery: numerical algorithms for extended, high-resolution modelling of vortex dynamics in two-dimensional, inviscid, incompressible flow, Comp. Phys. Rep. 10 (1989) 77–146.
[6] D.G. Dritschel, A fast hybrid algorithm for the simulation of fine-scale conservative fields on a sphere (submitted).
[7] D.G. Dritschel, M.H.P. Ambaum, A contour-advective semi-Lagrangian algorithm for the simulation of fine-scale conservative fields, Q. J. R. Meteorol. Soc. 123 (1997) 1097–1130 (DA97).
[8] D.G. Dritschel, C. Macaskill, The role of boundary conditions in the simulation of rotating, stratified turbulence, Geophys. Astrophys. Fluid Dyn. 92 (2000) 233–253.
[9] D.G. Dritschel, L.M. Polvani, A.R. Mohebalhojeh, The contour-advective semi-Lagrangian algorithm for the shallow water equations, Mon. Weather Rev. 127 (7) (1999) 1151–1165.
[10] D.G. Dritschel, R. Saravanan, Three-dimensional quasi-geostrophic contour dynamics, with an application to stratospheric vortex dynamics, Q. J. R. Meteorol. Soc. 120 (1994) 1267–1297.
[11] D.G. Dritschel, M. de la Torre Juárez, The instability and breakdown of tall columnar vortices in a quasi-geostrophic fluid, J. Fluid Mech. 328 (1996) 129–160.
[12] D.G. Dritschel, M. de la Torre Juárez, M.H.P. Ambaum, On the three-dimensional vortical nature of atmospheric and oceanic flows, Phys. Fluids 11 (6) (1999) 1512–1520.
[13] D.G. Dritschel, A. Viúdez, A balanced approach to modelling rotating stably-stratified flows J. Fluid Mech., 2003, in press.

[14] G.R. Flierl, On the instability of geostrophic vortices, J. Fluid Mech. 197 (1988) 349–388.
[15] J.-B. Flór, G.J.F. van Heijst, Stable and unstable monopolar vortices in a stratified fluid, J. Fluid Mech. 311 (1996) 257–287.
[16] B. Fornberg, A pseudospectral approach for polar and spherical geometries, SIAM J. Sci. Comput. 16 (1995) 1071–1081.
[17] E.J. Hopfinger, G.J.F. van Heijst, Vortices in rotating fluids, Ann. Rev. Fluid Mech. 25 (1993) 241–289.
[18] C.R. Koudella, D.G. Dritschel, G. McMullan, A parallel contour-advective semi-Lagrangian algorithm for the integration of the quasi-geostrophic fluid model, J. Comput. Phys., 2002 (submitted).
[19] B. Legras, D.G. Dritschel, Vortex stripping and the generation of high vorticity gradients in two-dimensional flows, Appl. Sci. Res. 51 (1993) 445–455.
[20] B. Legras, D.G. Dritschel, A comparison of the contour surgery and pseudo-spectral methods, J. Comput. Phys. 104 (1993) 287–302.
[21] S. Li, D. Montgomery, W.B. Jones, Two-dimensional turbulence with rigid circular walls, Theor. Comput. Fluid Dyn 9 (1997) 167–181.
[22] P.F. Linden, B.M. Boubnov, S.B. Dalziel, Source–sink turbulence in a rotating stratified fluid, J. Fluid Mech. 298 (1995) 81–112.
[23] C. Macaskill, Quasi-geostrophic three-dimensional flow in a cylinder, Phys. Lett. A 270 (3–4) (2000) 132–139.
[24] S.R. Maassen, H.J.H. Clercx, G.J.F. van Heijst, Decaying quasi-2D turbulence in a stratified fluid with circular boundaries, Europhys. Lett. 46 (1999) 339–345.
[25] J.C. McWilliams, J.B. Weiss, I. Yavneh, Anisotropy and coherent vortex structures in planetary turbulence, Science 264 (1994) 410–413.
[26] J.C. McWilliams, J.B. Weiss, I. Yavneh, The vortices of homogeneous geostrophic turbulence, J. Fluid Mech. 401 (1999) 1–26.
[27] M.V. Melander, J.C. McWilliams, N.J. Zabusky, Axisymmetrization and vorticity-gradient intensification of an isolated two-dimensional vortex through filamentation, J. Fluid Mech. 178 (1987) 137–159.
[28] M.V. Melander, N.J. Zabusky, J.C. McWilliams, Symmetric vortex merger in two dimensions: causes and conditions, J. Fluid Mech. 195 (1988) 303–340.
[29] L.M. Milne-Thomson, Theoretical Aerodynamics, fourth ed., Dover, New York, 1966.
[30] J.N. Reinaud, D.G. Dritschel, C.R. Koudella, The shape of vortices in quasi-geostrophic turbulence, J. Fluid Mech. 474 (2003) 175–191.
[31] R.K. Scott, D.G. Dritschel, L.M. Polvani, D.W. Waugh, Enhancement of Rossby wave breaking by steep potential vorticity gradients in the winter stratosphere, J. Atmos. Sci., 2003 (submitted).
[32] A. Viúdez, D.G. Dritschel, An explicit potential vorticity conserving approach to modelling nonlinear internal gravity waves, J. Fluid Mech. 458 (2002) 75–101.
[33] D.W. Waugh, D.G. Dritschel, The stability of filamentary vorticity in 2-dimensional geophysical vortex-dynamics models, J. Fluid Mech. 231 (1991) 575–598.